Research Article

Nano Research
2020, 13(11): 3068–3074

ISSN 1998-0124 CN 11-5974/O4
https://doi.org/10.1007/s12274-020-2974-7

Reaction environment self-modification on low-coordination Ni^{2+} octahedra atomic interface for superior electrocatalytic overall water splitting

Kaian Sun[1,2], Lei Zhao[1], Lingyou Zeng[1], Shoujie Liu[2], Houyu Zhu[3], Yanpeng Li[1], Zheng Chen[2], Zewen Zhuang[2], Zhaoling Li[4], Zhi Liu[1], Dongwei Cao[3], Jinchong Zhao[1], Yunqi Liu[1] (✉), Yuan Pan[1] (✉), and Chen Chen[2] (✉)

[1] *State Key Laboratory of Heavy Oil Processing, College of Chemical Engineering, China University of Petroleum (East China), Qingdao 266580, China*
[2] *Department of Chemistry, Tsinghua University, Beijing 100084, China*
[3] *College of Science, China University of Petroleum (East China), Qingdao 266580, China*
[4] *State Key Laboratory for Modification of Chemical Fibers and Polymer Materials, College of Textiles, Donghua University, Shanghai 201620, China*

Received: 2 March 2020 / **Revised:** 1 June 2020 / **Accepted:** 6 July 2020

ABSTRACT

Large scale synthesis of high-efficiency bifunctional electrocatalyst based on cost-effective and earth-abundant transition metal for overall water splitting in the alkaline environment is indispensable for renewable energy conversion. In this regard, meticulous design of active sites and probing their catalytic mechanism on both cathode and anode with different reaction environment at molecular-scale are vitally necessary. Herein, a coordination environment inheriting strategy is presented for designing low-coordination Ni^{2+} octahedra (L-Ni-8) atomic interface at a high concentration (4.6 at.%). Advanced spectroscopic techniques and theoretical calculations reveal that the self-matching electron delocalization and localization state at L-Ni-8 atomic interface enable an ideal reaction environment at both cathode and anode. To improve the efficiency of using the self-modification reaction environment at L-Ni-8, all of the structural features, including high atom economy, mass transfer, and electron transfer, are integrated together from atomic-scale to macro-scale. At high current density of 500 mA/cm^2, the samples synthesized at gram-scale can deliver low hydrogen evolution reaction (HER) and oxygen evolution reaction (OER) overpotentials of 262 and 348 mV, respectively.

KEYWORDS

atomic interface effect, overall water splitting, high current density, reaction environment self-modification, density functional theory

1 Introduction

Developing sustainable and environment-friendly energy technologies are of critical significance to meet the ever-increasing global energy demands. Electrochemical water splitting, which involves two key processes of cathodic hydrogen evolution reaction (HER) and anodic oxygen evolution reaction (OER), represents a promising alternative to convert electricity produced from intermittent natural resources into chemical energy. To make the water splitting process industrially more feasible, it is of great importance to design bifunctional transition metal electrocatalysts with low cost and high activity for both HER and OER [1].

As a typical second-row transition metal compound, MoS_2, normally in a thermodynamically stable 2H phase (2H MoS_2), has emerged as a competent candidate for HER in acidic media, owing to the edge sites of 2H MoS_2 possessing a close hydrogen atom adsorption free energy (ΔG_{H^*}) with that of the state-of-the-art Pt [2]. However, the 2H MoS_2 suffers from issues like scarce edge sites and semi-conductivity [3]. In contrast, 1T phase (1T MoS_2) has been considered as a competitive functional material for its metallic behavior and bulk H affinity; as a result, HER by 1T MoS_2 has rapidly attracted broad interest [4].

Compared with acidic HER, the HER and even OER suffer from more sluggish kinetics in the alkaline media, owing to complex H_2O dissociation and multistep electron transfer process at cathode and anode, respectively. To drive the two processes under alkaline media, a number of efficient strategies, such as morphology [5], composition [6], and interface engineering [7], have been proposed for designing bifunctional transition metal-based electrocatalysts towards reasonable OER and HER performance. Recent works illustrate that hybridizing MoS_2 with first-row transition metal (mainly Fe, Co, and Ni) compounds can simultaneously activate oxygen-containing intermediates and promote chemisorb H [8]. However, the transformation of charged intermediates between the two components only react at interface and easy to be blocked by larger sized molecules, decreasing the atomic efficiency and even results in undesirable side-reactions [9].

Single atom catalysts or atomic interface effects attract a great deal of effort, which can improve atom utilization and

Address correspondence to Yunqi Liu, liuyq@upc.edu.cn; Yuan Pan, panyuan@upc.edu.cn; Chen Chen, cchen@mail.tsinghua.edu.cn

catalytic properties for HER and OER. However, owing to the different reaction environments between HER and OER, pairing optimized active sites with different orbital structures in single system remains a challenge. For anode, transition metal atom in high oxidation states are preferred to activate the O-containing intermediates [10], whereas for cathode, a higher HER overpotential is required to dissociate the H_2O molecules, because the d-band centers (or Fermi level) of transition metal atom in high oxidation states are inherently much lower than the energy level of the lowest unoccupied molecular orbital (LUMO) or highest occupied molecular orbital (HOMO) of H_2O molecule [11]. Furthermore, the lack of effective synthesis strategy impedes the development of high-performance electrocatalysts for overall water splitting at large current density (usually greater than 500 mA/cm^2), which is beneficial to the commercialization of mass H_2 production.

Encouraged by the great potential of transition metal compounds, we synthesize low-coordination Ni^{2+} octahedra atomic interface (L-Ni-8) at gram-scale by inheriting the coordination environment of 1T MoS_2 to address these issues. All of the structural features are integrated together: (1) designing self-matching orbital electron delocalization and localization state on L-Ni-8 to provide an ideal reaction environment on both cathode and anode; (2) introducing L-Ni-8 into the bulk phase (basal plane) 1T MoS_2 at atomic scale at a high concentration (4.6 at.%); (3) enlarging the interlayer spacing of 1T MoS_2 at nanoscale to improve the accessibility of L-Ni-8 centers; (4) fabricating self-assembled nanosheets with array structure on conductive carbon cloth (CC) at macroscale to promote mass and electron transfer. Benefiting from the self-modified reaction environment at atomic interface and rationally designed structure on electrode materials, a performance superior to commercial noble metal electrocatalysts is achieved, especially at high current density of 500 mA/cm^2.

2 Results and discussion

2.1 Synthesis and characterization of the L-Ni-8 atomic interface

The details of gram-scale synthesis process are summarized in the experimental section (the digital photograph of products shown in Fig. 1(a)) [12]. X-ray diffraction (XRD) was used to identify the structure of the components of the samples before and after L-Ni-8 incorporation. For the sample with L-Ni-8 incorporated, apart from the peaks attributed to MoS_2 and CC, no diffraction peaks corresponding to Ni metals or its compounds were observed, suggesting a high dispersity of the Ni species. The diffraction peak of (100) plane of MoS_2 shifts to a lower angle, in contrast to the sample without Ni, in good agreement with density functional theory (DFT) structure for L-Ni-8 incorporation, yielding longer average atomic distance for Ni-Mo of 2.22 Å than pristine Mo–Mo of 2.21 Å (Fig. S1 in the Electronic Supplementary Material (ESM)). Meanwhile, according to Bragg equation, the interlayer spacing of the sample with L-Ni-8 incorporation is determined to 9.20 Å, which is smaller than the sample without L-Ni-8 and the sample intercalated by Ni^{2+} [13], indicating that the Ni species are embedded in the basal plane rather than within the shrunken interlayer space of MoS_2 (Fig. 1(b)). The high-angle annular dark-field scanning transmission electron microscopy (HAADF-STEM) image and corresponding elemental mapping images confirm that the Ni maps well overlap with Mo and S maps, with no aggregated Ni particles observed (Figs. 1(c)–1(f)). The microscopic structure of the MoS_2 after Ni incorporation

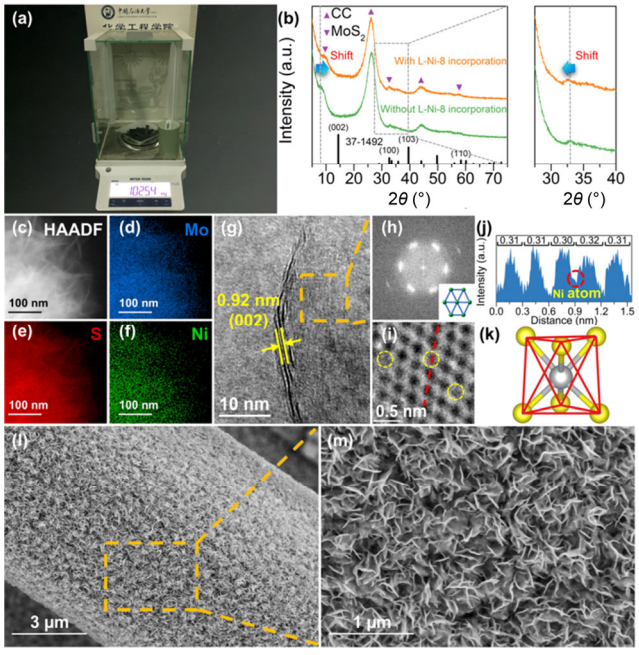

Figure 1 Structural characterizations. (a) Digital photograph. (b) XRD pattern. (c)–(f) HAADF-STEM and mapping images. (g) TEM image. (h) FFT pattern. (i) HRTEM image. (j) Line intensity profile. (k) Ni octahedral structure diagram. ((l) and (m)) SEM images.

was further investigated by high-resolution TEM (HRTEM). The measured interplanar distance of MoS_2 (002) lattice in the selected region agree well with XRD results (Fig. 1(g)). The fast Fourier transform (FFT) patterns on the basal plane of MoS_2 clearly show that six diffraction dots arise from six Mo atoms surrounding one Mo atom, which is assigned to the 1T phase of MoS_2 (Fig. 1(h)) [14].

Careful investigation of the line intensity profiles along the directions indicated by the lines in atom arrangement image shows that in-plane atom moves slightly closer to the side atom, in good agreement with the DFT structure (Figs. 1(i), 1(j), and Fig. S1 in the ESM). This is the direct evidence of the Ni atoms substituting in-plane Mo atoms in 1T MoS_2 bulk phase. In fact, in crystalline 1T MoS_2, each Mo atom is surrounded octahedrally by six S atoms ([MoS_6] octahedra). Thus, Ni atom can substitute in-plane Mo atom by inheriting a suitable octahedral octahedral coordination structure (Fig. 1(k)). The scanning electron microscopy (SEM) images show uniform MoS_2 nanosheets with a lateral size about 400 nm vertically grown on the surface of CC for the samples after 4.6 at.% Ni incorporation (determined by inductively coupled plasma optical emission spectrometry, in agreement with element mapping results above) (Figs. 1(l) and 1(m)). The unique three-dimensional (3D) cross-linked array structure with intricate pores and channels gives a Brunauer–Emmett–Teller specific surface area of 104 m^2/g and a pore diameter distributed in a wide range of 10–80 nm, highlighting the promotion of mass transfer (Fig. S2 in the ESM). Notably, with the high Ni content of 5.8 at.%, the nanosheets become much larger and even aggregate into non-uniform nanoflowers to the disadvantage of electrode kinetics (Fig. S3 in the ESM). The cubic phase NiS_2 (JCPDS card No. 88-1709) can be detected when Ni content reaches 7.1 at.% (Fig. S4 in the ESM).

The chemical state of samples was investigated by X-ray photoelectron spectroscopy (XPS). In the high-resolution spectral profile of Ni 2p region, the Ni $2p_{3/2}$ peaks are deconvoluted into three components at 854.3, 855.9, and 862.7 eV, which could be assigned to the Ni sulfides (Ni^{2+}), Ni oxides (or hydroxides), and the satellite peak, respectively (Fig. 2(a)).

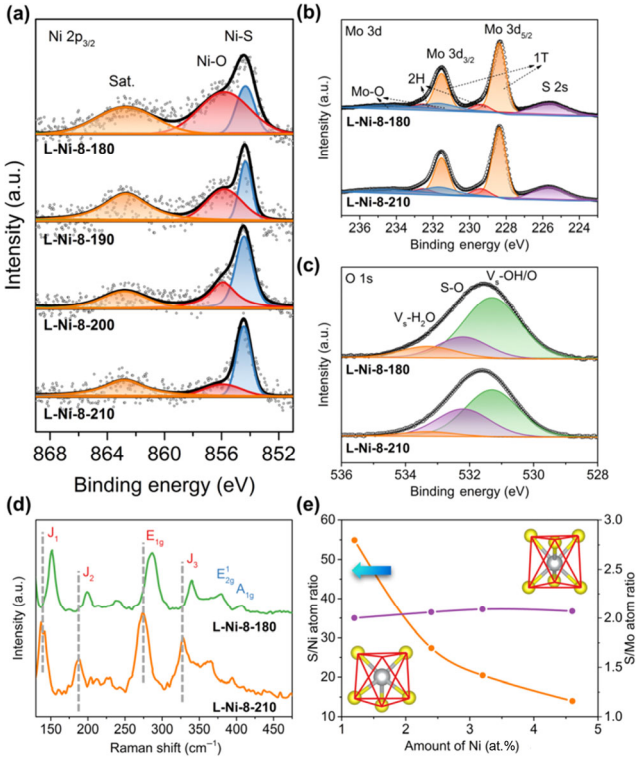

Figure 2 Chemical state characterizations. High-resolution XPS spectra in (a) Ni 2p, (b) Mo 3d, (c) O 1s regions. (d) Raman pattern. (e) Atomic ratio calculated by XPS.

Interestingly, the ratio of Ni sulfides to oxides/hydroxides becomes smaller with the decrease of synthesis temperature (the as-synthesized samples with and without Ni were denoted as L-Ni-8-*x* and L-Mo-8-*x*, respectively, where *x* presents the reaction temperature in the range of 1T MoS_2 formation, Figs. S5 and S6 in the ESM), whereas the chemical state of Mo presents indiscernible variation (~ 91% 1T MoS_2 with high-purity, Fig. 2(b)). This is in sharp contrast to the increase of oxidized or hydroxylated surface Mo species along with the temperature change without Ni (Fig. S7 in the ESM). The increased content of oxides or hydroxides of sample results from the adsorbed oxygen, hydroxyl groups, or water on surface sulfur vacancy (V_s) to maintain charge neutrality when the sample is exposed to air [15]. In comparison with L-Ni-8-210, the peaks of L-Ni-8-180 at 531.2 and 533.4 eV (attributed to surface-adsorbed oxygen or hydroxyl groups and water, respectively), are dominating (shown in O 1s regions, Fig. 2(c)) [16]. The surface adsorption at V_s is also consistent with the blue-shift of the J_1, J_2, J_3, and E_{1g} modes in Raman spectra resulting from the suppression of atomic vibrations by adsorbed species (Fig. 2(d)) [17]. A control experiment with a different amount of Ni incorporation exhibits that the decrease of S/Ni atomic ratio accompanies the increase of Ni, whereas S/Mo atomic ratio has no notable change (Fig. 2(e), Fig. S8 and Table S1 in the ESM). Therefore, the V_s can be confined around Ni^{2+} octahedra as L-Ni-8, and a decreased synthesis temperature can facilitate L-Ni-8 formation.

2.2 HER and OER performance of the L-Ni-8 atomic interface

A typical three-electrode setup was adopted to assess the HER performance under 1.0 M N_2-saturated KOH electrolyte. As shown in linear sweep voltammetry (LSV) curves, the L-Ni-8 has great impact on the HER performance. The L-Ni-8-180 with the maximum number of L-Ni-8 has the lowest overpotential of 48 mV at the current density of 10 mA/cm^2 among all samples. The present activity outperforms most of the recently reported HER catalysts, especially Mo/Fe/Co/Ni-based heterostructures (Table S2 in the ESM). In comparison to the state-of-the-art Pt/C benchmark, the L-Ni-8-180 exhibits a lower overpotential of 262 mV at a large current density of 500 mA/cm^2 (Fig. 3(a)). The inherent reaction process of the samples was evaluated by Tafel plots (Fig. 3(b)). The initial Tafel slope of 1T MoS_2 (L-Mo-8-180) is 131 mV/dec, which indicated that the rate-limiting step (RDS) is Volmer reaction. After L-Ni-8 introduction, the Tafel slopes show a dramatic decrease within the range of 40–120 mV/dec, suggesting the RDS change from the Volmer to the Heyrovsky reaction [18]. In other words, the initial water dissociation kinetic has been significantly accelerated by L-Ni-8 [19]. Meanwhile, L-Ni-8-180 exhibits the smallest charge-transfer resistance (R_{ct}) and the highest double-layer capacitance (C_{dl}) (Figs. S9–S11 in the ESM). Considering the comparable morphologies for all samples, the increased C_{dl} and decreased R_{ct} are associated with the proliferous active sites of L-Ni-8 (Fig. S12 in the ESM).

The OER performances were tested with a similar method used for HER. As expected, L-Mo-8-180 without Ni species exhibits a negligible OER activity. In sharp contrast, the samples with L-Ni-8 all exhibit significantly improved OER activities (Fig. 3(c)). A distinct oxidation peak can be found for all L-Ni-8-*x* samples, whereas it is not observed for L-Mo-8-180. It has been proved that spontaneous conversion of Ni oxidation state (from Ni^{2+} to Ni^{3+}) is considered prerequisites for the formation of active sites in most of Ni-based OER materials [20]. Similar to the HER system, the OER activity increases monotonously with increased L-Ni-8 content. Among all samples, the L-Ni-8-180 displays the highest oxidation peak with the lowest overpotential of 278 and 348 mV to reach a current density of 100 and 500 mA/cm^2, respectively. Such performances are significantly superior to those of the commercial RuO_2/CC and other reported state-of-the-art OER catalysts (Table S3 in the ESM). The excellent OER

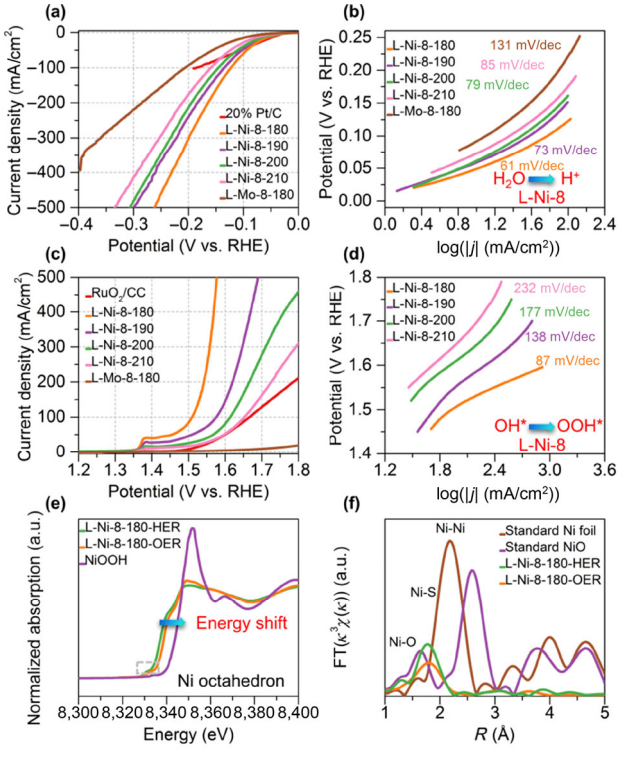

Figure 3 Electrochemical tests on HER and OER. ((a) and (b)) LSV and Tafel curves for HER, respectively. ((c) and (d)) LSV and Tafel curves for OER, respectively. (e) Ni K-edge XANES spectra. (f) FT-EXAFS spectra.

electrocatalytic activity of L-Ni-8-180 is attributed to the rich L-Ni-8, which delivers enhanced OER kinetics with the smallest Tafel slope of 87 mV/dec among all samples (Fig. 3(d)). The X-ray absorption near-edge structure (XANES) and extended X-ray absorption fine structure (EXAFS) of L-Ni-8-180 were measured to further clarify the structure evolution of L-Ni-8 after HER and OER tests (denoted as L-Ni-8-180-HER and L-Ni-8-180-OER, respectively). The spectral profile of Ni K-edge XANES of L-Ni-8-180-OER is very similar to that of L-Ni-8-180-HER, both with a small pre-edge peak, which is ascribed to the octahedral structures with six-coordinated Ni octahedra (Fig. 3(e)) [21], suggesting the presence of Ni-8 atomic interface after both HER and OER tests. The energy of rising edge on L-Ni-8-180-OER shifts to that of NiOOH sample confirming that the oxidation reaction took place on the catalyst surface to form high valence state Ni species during the OER. The Fourier transforms of the k^3-weighted EXAFS oscillations (FT-EXAFS) show the Ni–O peaks are negligible in L-Ni-8-180-HER and the Ni–S coordination number is 4.7, in contrast to 6 in saturated coordination Ni-8 (Table S4 in the ESM), indicating the peak intensities of Ni–O and Ni–S for L-Ni-8 in charge of OER and HER performance, respectively.

DFT calculations were carried out to further elucidate the influence of L-Ni-8 on alkaline HER and OER. Four types of 1T MoS_2 (002) models were examined, including pristine 1T MoS_2 (P-1T), 1T MoS_2 with saturated-coordination Ni (Ni-8-1T), 1T MoS_2 with low-coordination Mo (L-Mo-8-1T), and 1T MoS_2 with low-coordination Ni (L-Ni-8-1T). Heteroatom incorporation can promote the formation of low-coordination metal atom with confined V_s on the basal plane of 1T MoS_2, agreeing well with experimental results (Figs. S13 and S14 in the ESM). For alkaline HER, the adsorption strength of H_2O (ΔE_{H_2O}) and the energy barriers of H_2O dissociation (ΔG_{H_2O}) on different models were calculated (Fig. S15 in the ESM). The L-Ni-8-1T exhibits the lowest ΔE_{H_2O} and ΔG_{H_2O} (−0.58 and 0.60 eV, respectively), suggesting that L-Ni-8-1T could facilitate the RDS of alkaline HER (Figs. 4(a) and 4(b)). As shown in the partial charge density plot of L-Ni-8-1T for the band below the Fermi level (Fig. 4(c)), the electrons around L-Ni-8 become delocalization, leading to an upshift of all surface atoms towards the Fermi level, matching well with the energy level of the LUMO of H_2O (4a1) (Fig. 4(d)). The charge density difference plot further confirms a partial electron transfer from the surface to H_2O (Fig. 4(e)). When the LUMO of H_2O is filled, the bond order is decreased, thus facilitating the H_2O adsorption and dissociation for HER.

For alkaline OER, the four elementary pathways were considered, including M*→M–OH, M–OH→M–O, M–O→M–OOH, and M–OOH→O_2 (M* identified as adsorption site). As illustrated in the free energy diagrams (Fig. 4(f) and Fig. S16 in the ESM), the OH*/O* adsorption on L-Ni-8-1T is a thermodynamically feasible reaction, confirming the M–OH and M–O species could be more easily generated on L-Ni-8-1T. Compared with Ni-8-1T, the L-Ni-8-1T exhibits an extremely favorable OER kinetic with a lower overpotential by 0.80 eV in RDS, in good agreement with experimental results. According to Yang's principle, an ideal OER electrocatalyst should have a close to unity occupancy of the e_g orbital on surface cations, corresponding to a balance between the O–O bond formation step and the following proton-coupled electron transfer step [22]. Since the electro-negativity of O is larger than S, greater electron would be localized around the O atom after M–OH/M–O formation, increasing the valence state of Ni atom, as shown in Bader charge analysis (Fig. 4(g)). Compared with Ni-8-1T (Ni^{2+}) in a $t_{2g}^6e_g^2$ electron configuration, the L-Ni-8-1T with M–OH and M–O species under OER condition exhibits high valence Ni atom (Ni^{3+}) with a near-unity occupancy of the e_g orbital ($t_{2g}^6e_g^1$) (Fig. 4(h)). Theoretical calculations clearly

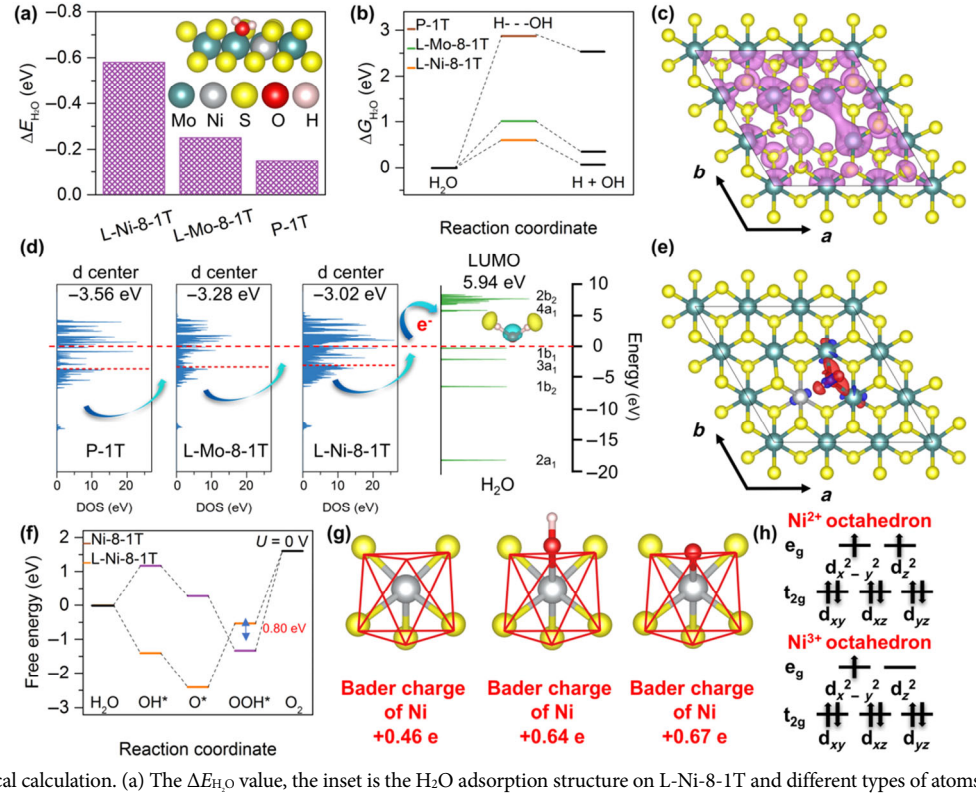

Figure 4 Theoretical calculation. (a) The ΔE_{H_2O} value, the inset is the H_2O adsorption structure on L-Ni-8-1T and different types of atoms represented by the different colored spheres. (b) The ΔG_{H_2O} value. (c) Partial charge density for the bands within 0.5 eV below Fermi level. The isosurface value is 0.005 e/Bohr^3. (d) Density of states. (e) Charge density difference. The isosurface value is 0.005 e/Bohr^3. (f) OER coordinate. (g) Bader charge. (h) Schematic illustration on electron orbits.

suggest that the delocalized electron around L-Ni-8 shifts the d-band center up towards the Fermi level under HER environment, and the localized electron around L-Ni-8 regulates the e_g orbital occupancy close to unity under OER environment. The electron delocalization and localization states enable low overpotentials for driving electron transfer from L-Ni-8 to the LUMO of H_2O at cathode and electron transfer from O-containing intermediates to L-Ni-8 at anode, respectively. Therefore, the self-matching orbital electron state on L-Ni-8 provides suitable reaction environments at both cathode and anode, leading to an improvement on H_2O redox activity under alkaline media.

2.3 Overall water splitting of the L-Ni-8 atomic interface

Other than L-Ni-8-180, Fe and Co doped 1T MoS_2 arrays prepared under the same conditions (denoted as L-Fe-8-180 and L-Co-8-180, respectively) were also employed as both cathode and anode for electrocatalytic overall water splitting. At a current density of 10 mA/cm, the L-Ni-8-180 gives a cell voltage of 1.51 V, which is much lower than that of L-Co-8-180 and L-Fe-8-180 (Fig. 5(a)). The inferior overall water splitting performances of L-Co-8-180 and L-Fe-8-180 may be attributed in part to their weak binding abilities toward proton for HER at cathode. The Ni-8 and L-Ni-8 exhibit the lowest ΔG_{H^*} value (0.41 and 0.69 eV), followed by that of in Co-8 and L-Co-8 (0.53 and 0.74 eV), Fe-8 (0.73 eV and 0.91 eV), respectively (Fig. 5(b) and Fig. S17 in the ESM). Notably, the L-Ni-8-180 shows quite a low cell voltage of 1.86 V at a large current density of 500 mA/cm^2. The HER, OER, and overall water splitting activities can keep stable for 12 h at such a large current density (Fig. 5(c) and Fig. S20 in the ESM). For cathode, the structure and surface morphology of L-Ni-8-180 are barely changed after the long-duration overall water splitting. For anode, although the structure of L-Ni-8-180 are slightly altered, no significant change in elements distribution are observed (Figs. S18 and S19 in the ESM).

To further confirm the basal plane doping and the bulk activity, the edge-oxidized samples (denoted as L-Ni-8-180-EO) were prepared as counterparts by partial oxidation in O_2-saturated aqueous solution over five days (Fig. S21 in the ESM) [23]. The LSV curves of L-Ni-8-180-EO show a slight shift with respect to pristine samples for both HER and OER, demonstrating that edge sites have no significant influence on electrocatalytic performance (Fig. 5(d)). Interestingly, different from a decay in HER activity, the partial oxidation can enhance OER activity and eliminate the oxidation peak, further confirming that high-oxidation-state Ni species are indeed highly active for OER.

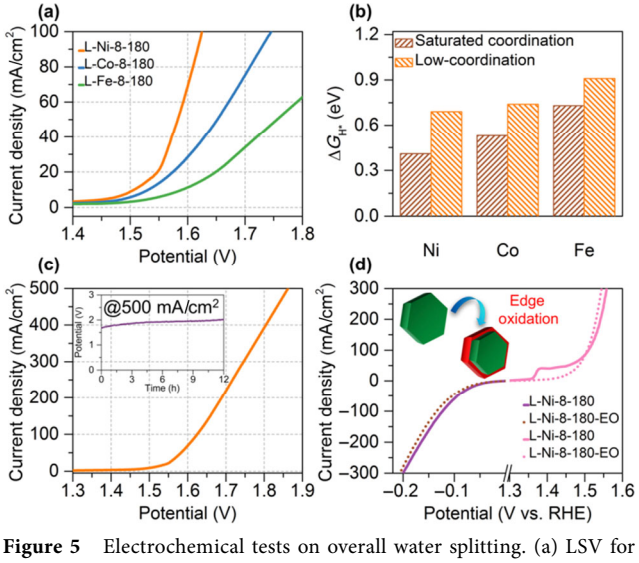

Figure 5 Electrochemical tests on overall water splitting. (a) LSV for overall water splitting. (b) The ΔG_{H^*} value. (c) LSV for overall water splitting at large current density, the inset is chronopotentiometric curve. (d) LSV for HER and OER.

3 Conclusion

In summary, we propose a concept of reaction environment self-modification at atomic interface for bifunctional transition metal-based electrocatalytic materials for HER and OER. When the L-Ni-8 is employed at cathode, the delocalized electron around L-Ni-8 can easily fill the lowest unoccupied molecular orbital of H_2O to decrease the bond order, and thereby accelerating its adsorption and dissociation in the RDS of HER in alkaline media. When the L-Ni-8 is employed at anode, the localized electron on O-containing intermediates can regulate the e_g orbital of L-Ni-8 occupancy close to unity, balancing the O–O bond formation step and the following proton-coupled electron transfer step in the RDS of OER. The optimized samples deliver a current density of 10 and 100 mA/cm^2 at an overpotential of 48 mV for the HER and 278 mV for OER, respectively. In a two-electrode system, cell voltages of 1.51 and 1.86 V were required for overall water splitting at current densities of 10 and 500 mA/cm^2, respectively. Our work here not only represents a promising strategy to gram-scale synthesis of robust bifunctional eletrocatalysts, but also provides fundamental insights from molecular-scale to macro-scale for designing electrocatalysts.

4 Experimental

4.1 Materials

L-cysteine (AR), sodium molybdate dihydrate (AR), urea (AR), nickel(II) nitrate hexahydrate (AR), cobalt(II) nitrate hexahydrate (AR), Iron(II) sulfate heptahydrate (AR), and polyethylene glycol (average molecular 1,000, CP) were purchased from Sinopharm Chemical Reagent Co., Ltd. (China). CC (WOS 1002, the thickness is 360 μm) was purchased from CeTech Co., Ltd. (China). All the above regents were used as received without any treatment. Ultrapure water (>18 MΩ) was used throughout all the experiments.

4.2 Synthesis

In a typical synthesis, sodium molydate dihydrate (as Mo source, 0.60 g), L-cysteine (as S source 0.65 g), urea (3.00 g), polyethylene glycol (140.00 g), and proper contents of transition metal salts were dissolved in aqueous solution of citric acid (pH = 3.5 ± 0.2, 160.00 g) with magnetic stirring for 10 min. Then, the well-dispersed solution was transferred into a 500 mL Teflon-lined stainless steel autoclave with about 20 pieces of CC (1 cm × 4 cm). The autoclave was heated for 20 h (heating rate 4 °C/min). After naturally cooled at room temperature, the as-prepared samples were washed subsequently with water and absolute ethanol several times, and then dried in vacuum at 60 °C for 12 h.

4.3 Materials characterization

XRD measurements were performed with a Panalytical X'pert PROX-ray diffractometer using Cu Kα radiation. Raman spectra were collected on a ThermoFisher DXR microscope with 532 nm laser excitation. TEM, HRTEM and element mapping analyses were taken on a JEOL JEM-2100F microscope at an acceleration

voltage of 200 kV. SEM images were recorded by a Hitachi S-4800 instrument operated at 5 kV. N_2 sorption experiments were performed at −196 °C on a Micromeritics ASAP 2420 instrument. The ICP-OES test was carried out on an Optima 8000 ICP-OES after the samples calcined in air at 600 °C and dissolved into HNO_3. Ni K-edge XANES and EXAFS were obtained at 1W1B station in BSRF (Beijing Synchrotron Radiation Facility, China) operated at 2.5 GeV with a maximum current of 250 mA. XPS measurements were carried out with a VG ESCALABMK II spectrometer with a monochromatic Al Kα source. In order to eliminate the influences of CC on MoS_2, the pure MoS_2 nanosheets were collected by ultrasonic exfoliation in a short time for XAFS and XPS tests.

4.4 Electrocatalytic measurement

Electrochemical performance was tested at room temperature by a Chenhua CHI 660D electrochemical workstation with a typical three-electrode setup, using a piece of self-supporting electrode as the working electrode (loading of ~ 0.01 g/cm^2), a graphite rod as the counter electrode and a saturated calomel electrode (SCE) as the reference electrode. The geometrical active area of working electrode was defined by the silicon rubber for immersing into electrolytes. LSV measurements were performed with a scan rate of 5 mV/s in N_2-saturated 1.0 M KOH electrolyte. All the potentials reported in our work were expressed vs. the reversible hydrogen electrode (RHE) with *iR* correction. For comparison, commercial 20% Pt/C and RuO_2 supported by CC with the same mass loading (0.01 g/cm^2) were also tested in same conditions.

4.5 Theoretical calculation details

Theoretical calculations were performed using Vienna ab initio simulation packages (VASP) based on DFT [24]. The interactions between core and valence electrons were described by the projector augmented wave (PAW) pseudopotentials [25]. The generalized gradient approximation (GGA) in the scheme of proposed by Perdew, Burke, and Ernzerhof (PBE) was adopted to express the electron exchange correlation with a cutoff energy of 400 eV, while the van der Waals effect and hydrogen bonding interactions were accounted for by the DFT-D2 method of Grimme with a 50 Å cutoff radius for pair interactions [26, 27]. Spin-polarization was considered for all the simulations. A 3 × 3 × 1 supercell with a 15 Å vacuum region was used to simulate the adsorption. The top layer together with the adsorbates and dopants were fully relaxed in all dimensions till all residual forces have declined below 0.02 eV Å^{-1} and the convergence of energy and forces were set to 1 × 10^{-5} eV. The Brillouin zone was sampled by the Monkhorst-Pack method with a 4 × 4 × 1 *k*-point grid. The climbing-image nudged elastic band (CI-NEB) method implemented in VASP was used to determine the diffusion energy barrier and the minimum energy pathways [28]. The OER elemental steps and Gibbs free energies were calculated based on the 4e$^-$ mechanism proposed by Norskov [29]. The kinetic energy barrier of the initial water dissociation step is applied as an activity descriptor for HER under alkaline condition, which can be calculated as follows

$$\Delta G_{H_2O} = G_{ts} - G_{ini}$$

where G_{ts} and G_{ini} are the free energy of the transient state and the initial state for water dissociation, respectively. The free energy is calculated using the equation

$$G = \Delta E + \mathrm{ZPE} + H - TS$$

where ZPE, *H*, *TS* are the zero-point energy, enthalpy, and entropy contributions (T = 298.15 K), respectively. And ΔE is the adsorption energy, defined as follows

$$\Delta E = E_{substrate+adsorbate} - E_{substrate} - E_{adsorbate}$$

The ΔG_{H^*} can be calculated as follows [30]

$$\Delta G_{H^*} = \Delta E + 0.24\ \mathrm{eV}$$

Acknowledgements

This work was supported by the National Natural Science Foundation of China (No. 21676300), the Shandong Provincial Natural Science Foundation (No. ZR2018MB035), the Fundamental Research Funds for the Central Universities (Nos. 19CX02008A and 16CX06007A), PetroChina Innovation Foundation (No. 2019D-5007-0401), Taishan Scholars Program of Shandong Province (No. tsqn201909065) and Tsinghua University Initiative Scientific Research Program.

Electronic Supplementary Material: Supplementary material (additional figures and tables) is available in the online version of this article at https://doi.org/10.1007/s12274-020-2974-7.

References

[1] Walter, M. G.; Warren, E. L.; McKone, J. R.; Boettcher, S. W.; Mi, Q. X.; Santori, E. A.; Lewis, N. S. Solar water splitting cells. *Chem. Rev.* **2010**, *110*, 6446–6473.

[2] Zou, X. X.; Zhang, Y. Noble metal-free hydrogen evolution catalysts for water splitting. *Chem. Soc. Rev.* **2015**, *44*, 5148–5180.

[3] Benck, J. D.; Hellstern, T. R.; Kibsgaard, J.; Chakthranont, P.; Jaramillo, T. F. Catalyzing the hydrogen evolution reaction (HER) with molybdenum sulfide nanomaterials. *ACS Catal.* **2014**, *4*, 3957–3971.

[4] Li, H. Y.; Chen, S. M.; Zhang, Y.; Zhang, Q. H.; Jia, X. F.; Zhang, Q.; Gu, L.; Sun, X. M.; Song, L.; Wang, X. Systematic design of superaerophobic nanotube-array electrode comprised of transition-metal sulfides for overall water splitting. *Nat. Commun.* **2018**, *9*, 2452.

[5] Yu, L.; Yang, J. F.; Guan, B. Y.; Lu, Y.; Lou, X. W. Hierarchical hollow nanoprisms based on ultrathin Ni-Fe layered double hydroxide nanosheets with enhanced electrocatalytic activity towards oxygen evolution. *Angew. Chem., Int. Ed.* **2018**, *57*, 172–176.

[6] Kuang, P. Y.; Tong, T.; Fan, K.; Yu, J. G. *In situ* fabrication of Ni-Mo bimetal sulfide hybrid as an efficient electrocatalyst for hydrogen evolution over a wide pH range. *ACS Catal.* **2017**, *7*, 6179–6187.

[7] Hu, J.; Zhang, C. X.; Jiang, L.; Lin, H.; An, Y. M.; Zhou, D.; Leung, M. K. H.; Yang, S. H. Nanohybridization of MoS_2 with layered double hydroxides efficiently synergizes the hydrogen evolution in alkaline media. *Joule* **2017**, *1*, 383–393.

[8] Wang, T. Y.; Nam, G.; Jin, Y.; Wang, X. Y.; Ren, P. J.; Kim, M. G.; Liang, J. S.; Wen, X. D.; Jang, H.; Han, J. T. et al. NiFe (Oxy) hydroxides derived from NiFe disulfides as an efficient oxygen evolution catalyst for rechargeable Zn–air batteries: The effect of surface S residues. *Adv. Mater.* **2018**, *30*, 1800757.

[9] Chen, Z. X.; Leng, K.; Zhao, X. X.; Malkhandi, S.; Tang, W.; Tian, B. B.; Dong, L.; Zheng, L. R.; Lin, M.; Yeo, B. S. et al. Interface confined hydrogen evolution reaction in zero valent metal nanoparticles-intercalated molybdenum disulfide. *Nat. Commun.* **2017**, *8*, 14548.

[10] Liu, Y.; Ying, Y. R.; Fei, L. F.; Liu, Y.; Hu, Q. Z.; Zhang, G. G.; Pang, S. Y.; Lu, W.; Mak, C. L.; Luo, X. et al. Valence engineering via selective atomic substitution on tetrahedral sites in spinel oxide for highly enhanced oxygen evolution catalysis. *J. Am. Chem. Soc.* **2019**, *141*, 8136–8145.

[11] Deng, J.; Li, H. B.; Wang, S. H.; Ding, D.; Chen, M. S.; Liu, C.; Tian, Z. Q.; Novoselov, K. S.; Ma, C.; Deng, D. H. et al. Multiscale structural and electronic control of molybdenum disulfide foam for highly efficient hydrogen production. *Nat. Commun.* **2017**, *8*, 14430.

[12] Sun, K. A.; Liu, Y. Q.; Pan, Y.; Zhu, H. Y.; Zhao, J. C.; Zeng, L. Y.; Liu, Z.; Liu, C. G. Targeted bottom-up synthesis of 1T-phase MoS_2 arrays with high electrocatalytic hydrogen evolution activity by

simultaneous structure and morphology engineering. *Nano Res*. **2018**, *11*, 4368–4379.

[13] Attanayake, N. H.; Thenuwara, A. C.; Patra, A.; Aulin, Y. V.; Tran, T. M.; Chakraborty, H.; Borguet, E.; Klein, M. L.; Perdew, J. P.; Strongin, D. R. Effect of intercalated metals on the electrocatalytic activity of 1T-MoS_2 for the hydrogen evolution reaction. *ACS Energy Lett*. **2018**, *3*, 7–13.

[14] Fang, Y. Q.; Pan, J.; He, J. Q.; Luo, R. C.; Wang, D.; Che, X. L.; Bu, K. J.; Zhao, W.; Liu, P.; Mu, G. et al. Structure Re-determination and superconductivity observation of bulk 1T MoS_2. *Angew*. *Chem*. **2018**, *130*, 1246–1249.

[15] Fominykh, K.; Feckl, J. M.; Sicklinger, J.; Döblinger, M.; Böcklein, S.; Ziegler, J.; Peter, L.; Rathousky, J.; Scheidt, E. W.; Bein, T. et al. Ultrasmall dispersible crystalline nickel oxide nanoparticles as high-performance catalysts for electrochemical water splitting. *Adv*. *Funct*. *Mater*. **2014**, *24*, 3123–3129.

[16] Zhuang, L. Z.; Ge, L.; Yang, Y. S.; Li, M. R.; Jia, Y.; Yao, X. D.; Zhu, Z. H. Ultrathin iron-cobalt oxide nanosheets with abundant oxygen vacancies for the oxygen evolution reaction. *Adv*. *Mater*. **2017**, *29*, 1606793.

[17] Cho, K.; Min, M.; Kim, T. Y.; Jeong, H.; Pak, J.; Kim, J. K.; Jang, J.; Yun, S. J.; Lee, Y. H.; Hong, W. K. et al. Electrical and optical characterization of MoS_2 with sulfur vacancy passivation by treatment with alkanethiol molecules. *ACS Nano* **2015**, *9*, 8044–8053.

[18] Feng, J. X.; Wu, J. Q.; Tong, Y. X.; Li, G. R.; Efficient hydrogen evolution on Cu nanodots-decorated Ni_3S_2 nanotubes by optimizing atomic hydrogen adsorption and desorption. *J*. *Am*. *Chem*. *Soc*. **2018**, *140*, 610–617.

[19] Pan, Y.; Sun, K. A.; Liu, S. J.; Cao, X.; Wu, K. L.; Cheong, W. C.; Chen, Z.; Wang, Y.; Li, Y.; Liu, Y. Q. et al. Core-shell ZIF-8@ZIF-67-derived CoP nanoparticle-embedded N-doped carbon nanotube hollow polyhedron for efficient overall water splitting. *J*. *Am*. *Chem*. *Soc*. **2018**, *140*, 2610–2618.

[20] Zhao, Y. F.; Jia, X. D.; Chen, G. B.; Shang, L.; Waterhouse, G. I. N.; Wu, L. Z.; Tung, C. H.; O'Hare, D.; Zhang, T. R. Ultrafine NiO nanosheets stabilized by TiO_2 from monolayer NiTi-LDH precursors: An active water oxidation electrocatalyst. *J*. *Am*. *Chem*. *Soc*. **2016**, *138*, 6517–6524.

[21] Niemann, W.; Clausen, B. S.; Topsøe, H. X-Ray absorption studies of the Ni environment in Ni-Mo-S. *Catal*. *Lett*. **1990**, *4*, 355–363.

[22] Suntivich, J.; May, K. J.; Gasteiger, H. A.; Goodenough, J. B.; Shao-Horn, Y. A perovskite oxide optimized for oxygen evolution catalysis from molecular orbital principles. *Science* **2011**, *334*, 1383–1385.

[23] Sun, K. A.; Zeng, L. Y.; Liu, S. H.; Zhao, L.; Zhu, H. Y.; Zhao, J. C.; Liu, Z.; Cao, D. W.; Hou, Y. C.; Liu, Y. Q. et al. Design of basal plane active MoS_2 through one-step nitrogen and phosphorus co-doping as an efficient pH-universal electrocatalyst for hydrogen evolution. *Nano Energy* **2019**, *58*, 862–869.

[24] Kresse, G.; Furthmüller, J. Efficient iterative schemes for *ab initio* total-energy calculations using a plane-wave basis set. *Phys*. *Rev*. *B* **1996**, *54*, 11169–11186.

[25] Blöchl P. E. Projector augmented-wave method. *Phys*. *Rev*. *B* **1994**, *50*, 17953–17979.

[26] Perdew, J. P.; Burke, K.; Ernzerhof, M. Generalized gradient approximation made simple [Phys. Rev. Lett. 77, 3865 (1996)]. *Phys*. *Rev*. *Lett*. **1997**, *78*, 1396.

[27] Grimme, S.; Antony, J.; Ehrlich, S.; Krieg, H. A consistent and accurate *ab initio* parametrization of density functional dispersion correction (DFT-D) for the 94 elements H-Pu. *J*. *Chem*. *Phys*. **2010**, *132*, 154104.

[28] Henkelman, G.; Uberuaga, B. P.; Jónsson, H. A climbing image nudged elastic band method for finding saddle points and minimum energy paths. *J*. *Chem*. *Phys*. **2000**, *113*, 9901–9904.

[29] Rossmeisl, J.; Qu, Z. W.; Zhu, H.; Kroes, G. J.; Nørskov, J. K. Electrolysis of water on oxide surfaces. *J*. *Electroanal*. *Chem*. **2007**, *607*, 83–89.

[30] Nørskov, J. K.; Bligaard, T.; Logadottir, A.; Kitchin, J. R.; Chen, J. G.; Pandelov, S.; Stimming, U. Trends in the exchange current for hydrogen evolution. *J*. *Electrochem*. *Soc*. **2005**, *152*, J23–J26.